*Kovove Mater. 63 2025 15–32*
*DOI: 10.31577/km.2025.1.15*



# Tensile and fracture behaviour of cryorolled and post-annealed Al 6351 alloy: Experiments and simulations

Pankaj Rawat, Amit Joshi*, Ashutosh Gupta

*Department of Mechanical Engineering, Govind Ballabh Pant Institute of Engineering and Technology, Pauri, Uttarakhand 246194, India*

Received 2 October 2024, received in revised form 18 November 2024, accepted 3 December 2024

**Abstract**

Al 6351 is extensively utilised in aerospace and automotive applications due to its excellent mechanical properties. These properties can be further enhanced through a combination of work hardening via cryorolling (CR) and precipitation hardening via post-annealing (PA) treatment, making the resulting Al 6351 alloy more suitable for various structural applications in these industries. For CR treatment, the solution-treated (ST) sample of Al 6351 alloy was exposed to a true strain of 2.3, and the PA was carried out for CR Al 6351 alloy at 100 to 350 °C temperature range for 1 hour. Despite the potential of CR and PA to improve mechanical properties, their effectiveness has not been reported so far. The mechanical behaviour of the different processing conditions was investigated using tensile and fracture toughness tests. The CR sample annealed at 100 °C showed a peak hardness of (90 HV), tensile (UTS of 306 MPa), and fracture toughness parameters ($K_Q = 11.2$ MPa $\sqrt{m}$, $K_{ee} = 20.9$ MPa $\sqrt{m}$, and $J$ integral $= 13.8$ kJ m$^{-2}$). The fracture toughness of cryorolled + annealed samples remain consistent until the annealing temperature of 200 °C but shows a sharp decline beyond 200 °C.

K e y w o r d s: severe plastic deformation, aluminium alloy, fracture toughness, structure-property correlation

## 1. Introduction

Al 6351 is a precipitation-hardenable alloy that finds extensive use in the automotive, aerospace, and piping industries [1, 2] owing to its desirable combination of mechanical properties, including high specific strength, fracture, and corrosion resistance. The shift toward greener technologies in these industries necessitates using lightweight alloys with low density and high specific strength [3, 4]. The specific strength of the heat-treatable Al alloy, such as Al 6351, can be enhanced by utilising various strengthening mechanisms, such as solid solution strengthening, precipitation hardening, and grain boundary strengthening [5]. Among the different approaches for strengthening, the processing method called the severe plastic deformation (SPD) process, combined with heat treatment, has gained widespread attention due to its excellent capability to enhance mechanical properties in Al alloys [6, 7].

The SPD processes were first coined in 1950 [6] and have been successfully employed to enhance the mechanical characteristics of various materials like aluminium alloys [6], steel [8, 9], magnesium alloys [10], etc. The SPD process leads to the formation of ultrafine (UFG) microstructure, typically in the range of 100 nm–1 μm, which increases the mechanical properties [11]. Most of these processes, like multi-axial forging (MAF) and equal-channel angular pressing (ECAP), require sophisticated equipment or intricate die [7], which increases the initial and maintenance costs. However, cryorolling (CR) treatment is one of the few SPD processes that does not necessitate complicated and expensive dies [5]. The CR treatment can also be readily integrated into a continuous and automated manufacturing line. Another advantage of the CR process is that the final output of the CR treatment is in sheet form, which is significant considering the fact that approximately 46 % of the aluminium alloys in structural and aerospace applications are in the

*Corresponding author: e-mail address: amitiitrebsd@gmail.com

form of sheets [12]. The cryogenic temperature in the CR suppresses the dislocation cross-slip movement, thereby increasing the dislocation density [6]. These areas of high dislocation density act as an obstacle to the dislocation motion and, therefore, enhance the mechanical characteristics of the alloy. Panigrahi and Jayaganthan [13] studied the influence of CR treatment (90 % thickness reduction) on Al-Mg-Si alloy and reported an increment of 123 % in UTS. While the tensile strength typically increases after CR, this increase is often accompanied by a significant decrease in ductility [13, 14]. This reduced ductility in the CR samples can make such alloys unsuitable for application in different industries. Consequently, addressing the low ductility is crucial to make material viable for structural application, and annealing is widely acknowledged as an effective method to enhance both ductility and strength in heat-treatable Al alloys. However, despite these numerous advantages of the CR, its effectiveness in enhancing mechanical properties has not been reported.

In addition to the tensile properties, fracture toughness is crucial, particularly for aerospace applications, where it works as a basis for the damage-tolerant approach. Consequently, several researchers have investigated the fracture toughness behaviour of SPD aluminium alloy. Gairola et al. [6] and Kapil et al. [7] have explored the fracture toughness of CR and MAF for Al 8090 alloy, respectively, and reported an increase of 40.38 % for CR with 90 % thickness reduction and 72.26 % after MAF of 6 cycles. Similar findings have been reported for SPD of different aluminium alloys, such as AA5052 [15] and Al 6082 [16]. The finite element analysis (FEA) can be essential for predicting crack growth for fracture toughness behaviour. The crack is defined in the conventional FEM by aligning the mesh edge with the crack edge. As the crack advances, it becomes essential to utilise conformal meshing to align the mesh edge with the crack edge. This increases the computational resources needed for simulating crack growth, such as in the simulation of a three-point bend test. The extended finite element analysis (XFEM) method permits crack growth through the mesh, eliminating the necessity for conformal meshing. The XFEM method has been effectively utilised to predict crack propagation in various aluminium alloys, including Al 6061 [17, 18] and Al 7075 alloy [19]. However, the fracture toughness behaviour of CR Al 6351 alloy using experiment and simulation has not been reported.

Thiyagarajan and Gopinath [20] examined the influence of ECAP (single pass) on Al 6351 and reported an increase of 54.36 % in UTS. However, studies on the CR Al 6351 alloy are scarce in the literature. Hence, the current study investigates the effect of the formation of UFG microstructure by cryorolling and the influence of annealing treatment on cryorolled Al 6351 alloy. The mechanical properties of Al 6351 were characterised by hardness, tensile and three-point bend (3-PB) tests, and the results obtained are correlated with the microstructure characterised by scanning electron microscopy (SEM), transmission electron microscopy (TEM) and optical microscopy.

## 2. Experimental procedure

Al 6351 alloy in T6-treated condition was acquired from "Tremor Alloy Mumbai, India" in the form of 100 mm × 80 mm × 32 mm sheets. The procured sheets were machined into 60 mm × 40 mm × 10 mm prismatic sheets. These sheets were solution treated (ST) by placing them in an oil bath furnace at a temperature of 540 ℃ for 2 hours and subsequent water quenching to get a homogeneous microstructure and relieve the residual stress in the sheets due to machining. The ST samples were put through the CR process to achieve a thickness reduction of 90 %. CR process was implemented by sinking the ST samples in liquid nitrogen for 25 minutes before every rolling pass. This ensures a uniform temperature of –196 ℃ across samples during cryogenic deformation. Two high-rolling mills are used to carry out the multi-pass unidirectional CR process. In each pass, the thickness of the strip is reduced by 10 %. This process is repeated until the true stress of 2.3 is achieved, where true strain is defined as:

$$\begin{aligned}\text{True strain } \varepsilon_{\text{true}} &= \ln\left(1-\varepsilon_{\text{engg}}\right)\\ &= \ln\left(\frac{\text{final thickness}}{\text{initial thickness}}\right). \quad (1)\end{aligned}$$

Annealing of CR processed samples was carried out at temperatures ranging from 100 to 350 ℃, aiming to investigate the impact of post-annealing (PA) on the microstructure and fracture toughness behaviour of CR Al 6351 alloy. The designation of the processing condition is shown in Table 1.

### 2.1. Sample preparation

The mechanical behaviour of Al 6351 alloy was examined using Vickers hardness, tensile, and three-point bend tests. The microstructural and precipitation behaviour was investigated using optical, TEM (transmission electron microscopy), and XRD (X-ray diffraction) analysis. "H25 K-S Tinius Olsen" machine operated at a constant crosshead speed, and a strain rate of $5 \times 10^{-4}\,\text{s}^{-1}$ was used to assess the tensile behaviour of cryorolled and post-annealed Al 6351 samples. Samples for the tensile test were machined as per ASTM E8 subsize standard in the rolling direction [6]. The specification of the tensile specimen is displayed in Fig. 1a. Vickers hardness test apparatus (with a

Table 1. Designation used in the current study

| Abbreviation | Meaning |
|---|---|
| ST | Solution treatment at 540 °C for 2 h |
| CR | Cryorolled to a true strain of 2.3 |
| CR + PA | Cryorolled and subsequent post-annealing |
| CR + 100 °C | Cryorolled and subsequent annealing at 100 °C |
| CR + 150 °C | Cryorolled and subsequent annealing at 150 °C |
| CR + 200 °C | Cryorolled and subsequent annealing at 200 °C |
| CR + 250 °C | Cryorolled and subsequent annealing at 250 °C |
| CR + 300 °C | Cryorolled and subsequent annealing at 300 °C |
| CR + 350 °C | Cryorolled and subsequent annealing at 350 °C |

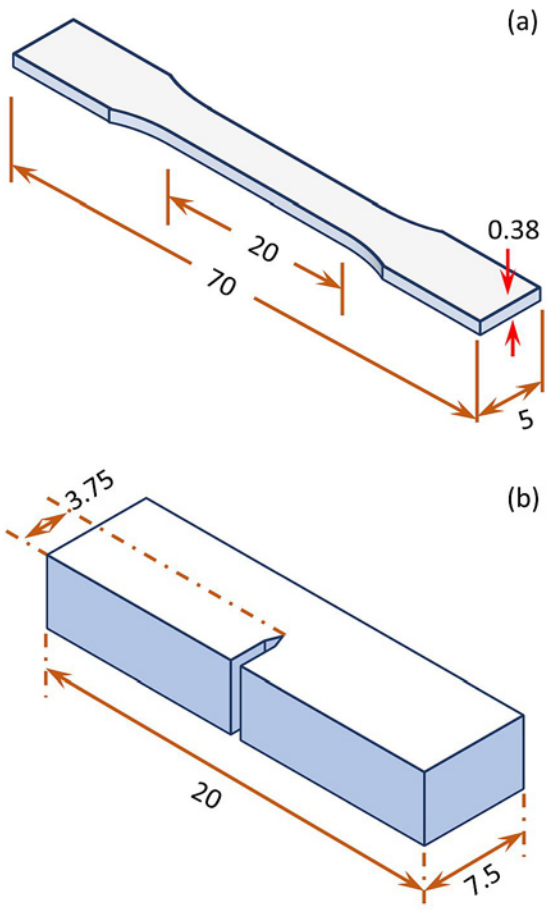


Fig. 1. Specifications of (a) tensile specimen and (b) 3-PB test samples (all dimensions in mm).

load of 5 kg and a dwell time of 15 seconds) was used to carry out the hardness test.

The samples for microstructural characterisation were polished using emery paper of different grades in the range of 320 to 2500 and finished using a polishing cloth with MgO powder. These samples were treated with Poulten's regents to improve the contrast of grain boundaries and observed under the "Leica DMI 5000" microscope. Transmission electron microscopy (TEM) was performed using "Philips CM 12" machine. TEM samples were made by polishing the samples with 320, 800, 1200, and 1500 grit emery paper, thinning the sample up to 100 µm and then finishing by "twin-jet-electro-polisher machine" using methanol (75 %) and nitric acid (25 %) at –30 °C temperature. The fracture toughness was examined using the 3-PB test, which SEM followed to observe the fractograph of the fracture surface. Fracture toughness testing was carried out using a distinct fitment of the 3-PB test on a tensile testing machine (H25K-S Tinius Olsen). 3-PB test specimens were machined as per ASTM 399 standard [21]. The sample specification for the 3-PB test is presented in Fig. 1b.

## 3. Results and discussion

### 3.1. Microstructure characterisation

Optical microscopy was used for material characterisation in the solution-treated, cryorolled, and post-annealing conditions. Solution-treated (ST) samples show coarse equiaxed microstructure with grain size in the 100–150 µm range. The grain size was calculated using the line intercept method in *Image J 1.53 software*. Cryorolling with a thickness reduction of 90 % leads to the formation of fine elongated grain along the rolling direction. Annealing of cryorolled samples leads to an upsurge in grain size and subgrain formation due to dislocation rearrangement. As the annealing temperature increases, there is a corresponding increase in the degree of recrystallisation and grain size. Annealing of samples up to a temperature of 200 °C does not show any significant variation; the microstructure remains elongated, but grain size increases slightly, as displayed in Figs. 2c,d; however, as the annealing temperatures rise to 350 °C, the elongated grain structure becomes moderately coarse and akin to the equiaxed microstructure in the ST sample. This change can be attributed to the recrystallisation phenomenon and rearrangement of dislocation and subcells, as stated in

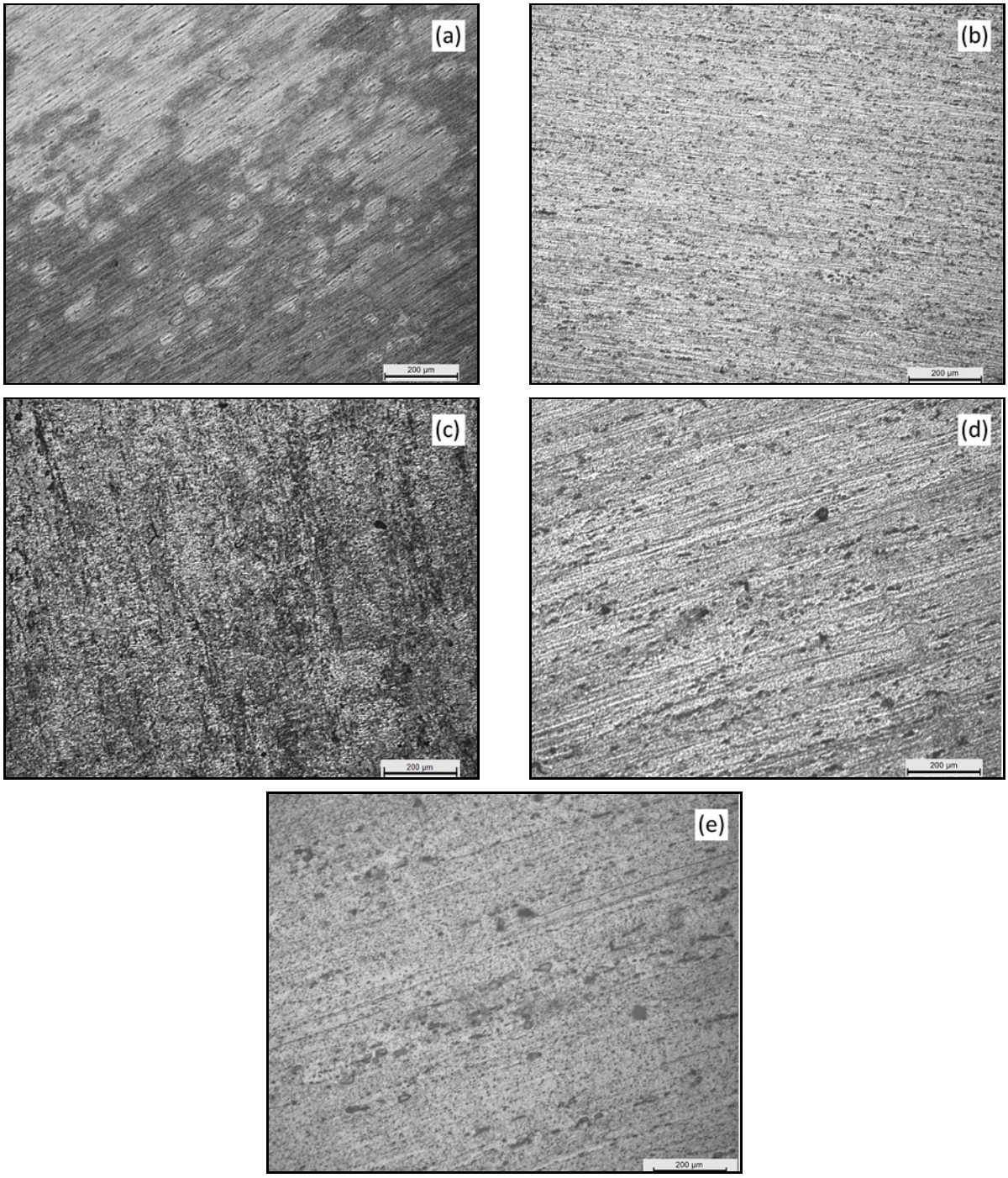


Fig. 2. Optical micrographs (a) ST, (b) CR, (c) CR + 100 °C, (d) CR + 150 °C, and (e) CR + 350 °C.

numerous formerly published works [6, 22]. However, the distinction between grain boundaries and grain interior is a bit vague in the OM, leading to errors in the grain size measurement in the deformed and PA specimens.

### *3.1.1. EBSD analysis*

Since the OM failed to accurately measure the grain size in the deformed and PA specimens, the grain size measurement of the ST, CR, and PA specimens in different annealing temperatures was measured using EBSD analysis, as shown in Fig. 3. As observed using the OM, the EBSD micrograph of ST specimen also showed the equiaxed microstructure with an average grain size of 102 µm. The CR treatment on the ST specimen led to the evolution of elongated grains along the rolling direction, as shown in Fig. 3b. Furthermore, the CR specimen also showed a significant number of subgrains with low-angle grain boundaries

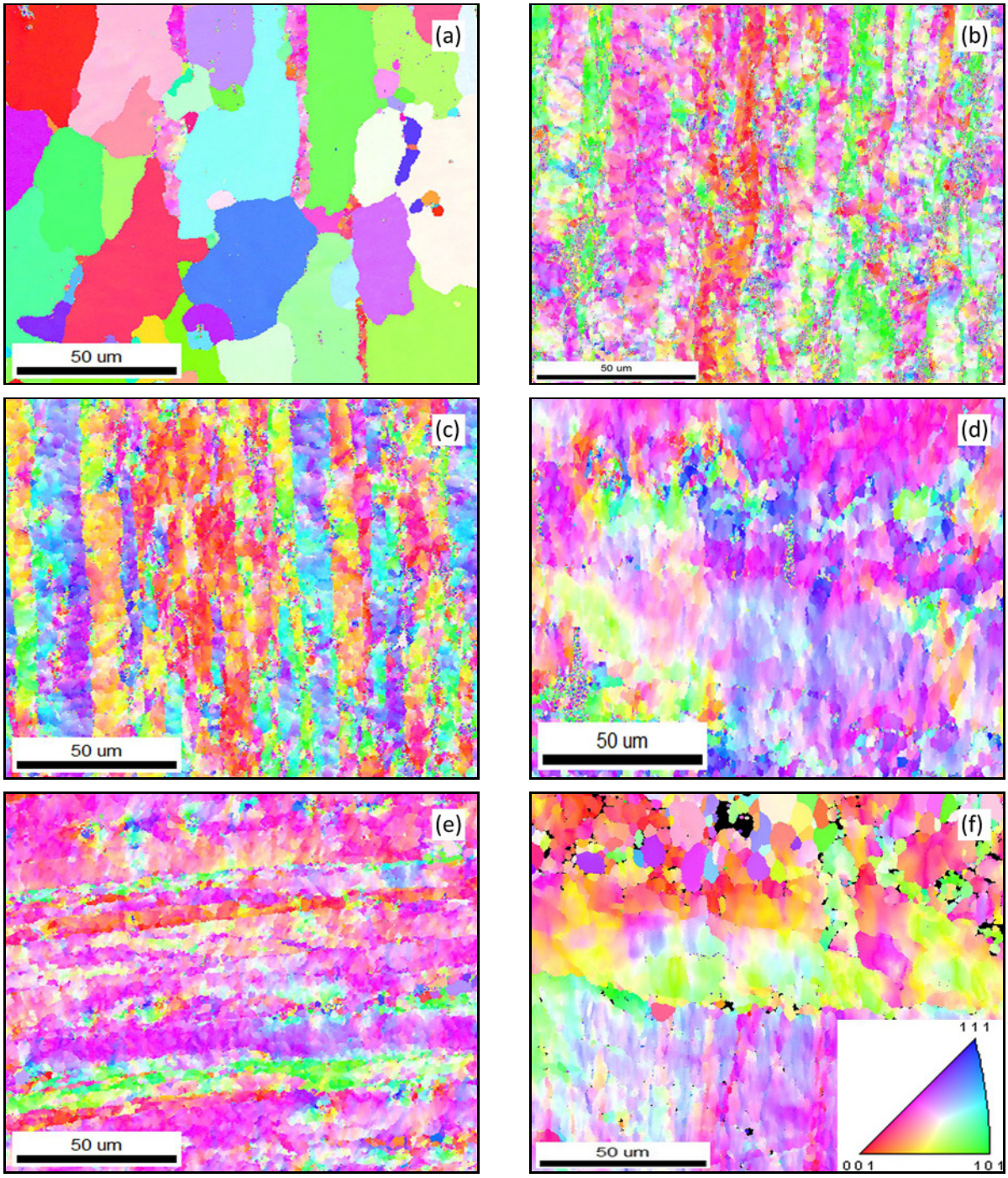


Fig. 3. Inverse pole figure (IPF) map for (a) ST, (b) CR, (c) CR + 100 °C, (d) CR + 150 °C, (e) CR + 250 °C, and (f) CR + 350 °C.

(LAGB), which can be attributed to the grain refinement and suppression of dynamic recovery during the CR process. The cryogenic temperature suppresses the dynamic recovery and thereby increases the dislocation density of the CR specimen [7]. The PA samples at 100 °C temperature showed similar elongated microstructures along the rolling direction, with slightly larger grain sizes and higher high-angle grain boundaries (HAGB) fractions. This slight microstructure recovery can be attributed to the recovery and recrystallisation during the annealing treatment. The PA specimen shows the subgrain formation due to the rearrangement and annihilation of the dislocation densities as the PA temperature increases to 150 and 250 °C, as shown in Figs. 3d,e, respectively, the microstructure is significantly recovered, and the subgrains are

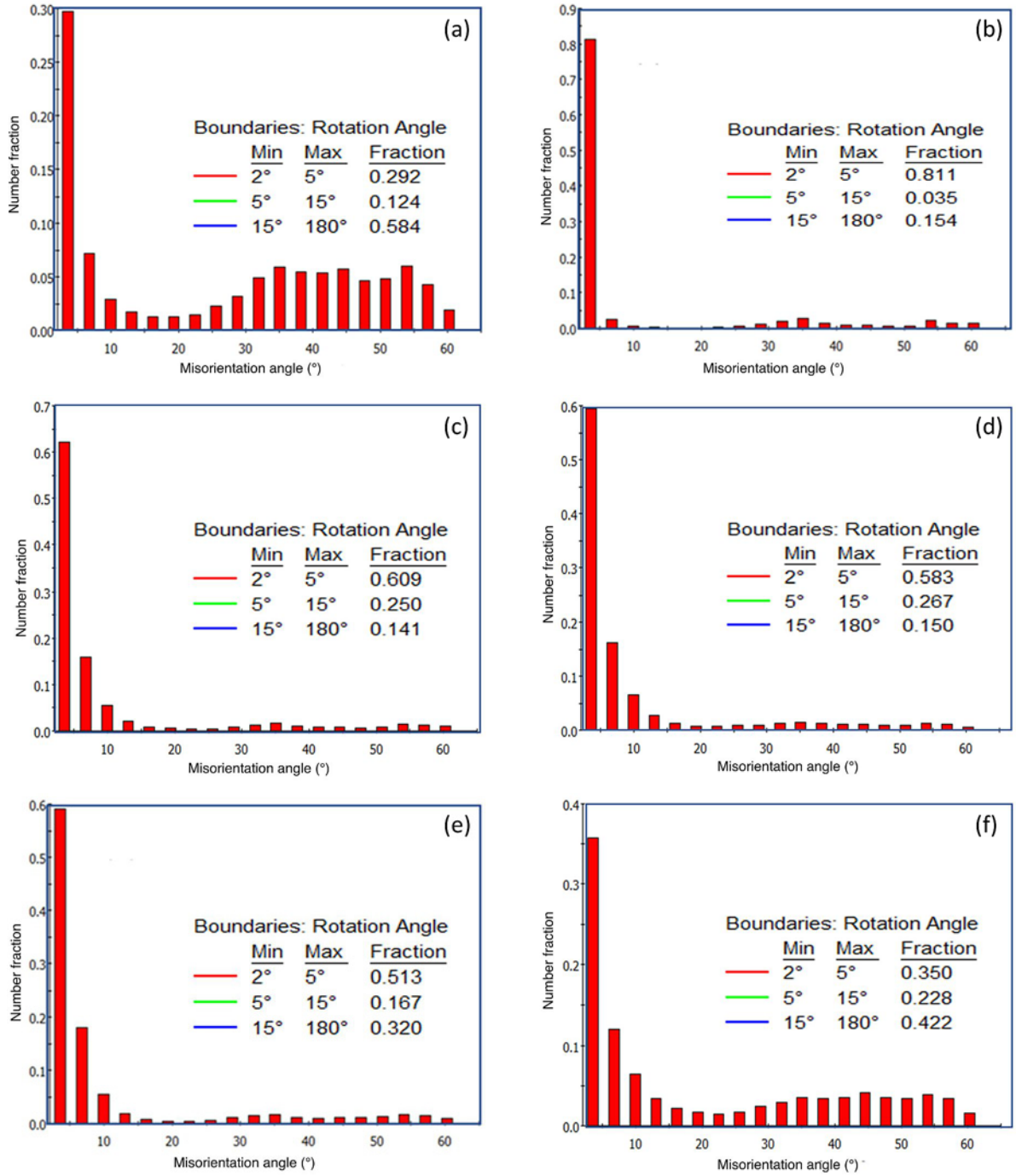


Fig. 4. Misorientation angle distribution for (a) ST, (b) CR, (c) CR + 100 °C, (d) CR + 150 °C, (e) CR + 250 °C, and (f) CR + 350 °C.

reduced substantially. However, the CR + 150 °C grain structure and CR + 250 °C remain elongated along the rolling direction. On further increase in PA temperature to 350 °C, the microstructure is converted into the mixture of equiaxed and elongated microstructure, with the fraction of equiaxed microstructure being higher than the elongated microstructure. Most of the subgrains and dislocation density generated during the SPD process are recovered during PA treatment. However, it is interesting to note that despite the recovered equiaxed microstructure in the CR + 350 °C specimen, the grain size of the PA samples is still higher compared to the ST specimen.

The misorientation distribution of ST, CR, and PA samples is shown in Figs. 4a–f, respectively. The misorientation angle distribution of the ST specimen showed the presence of a higher fraction of high-angle grain boundaries (HAGB) of 0.584 and a low fraction

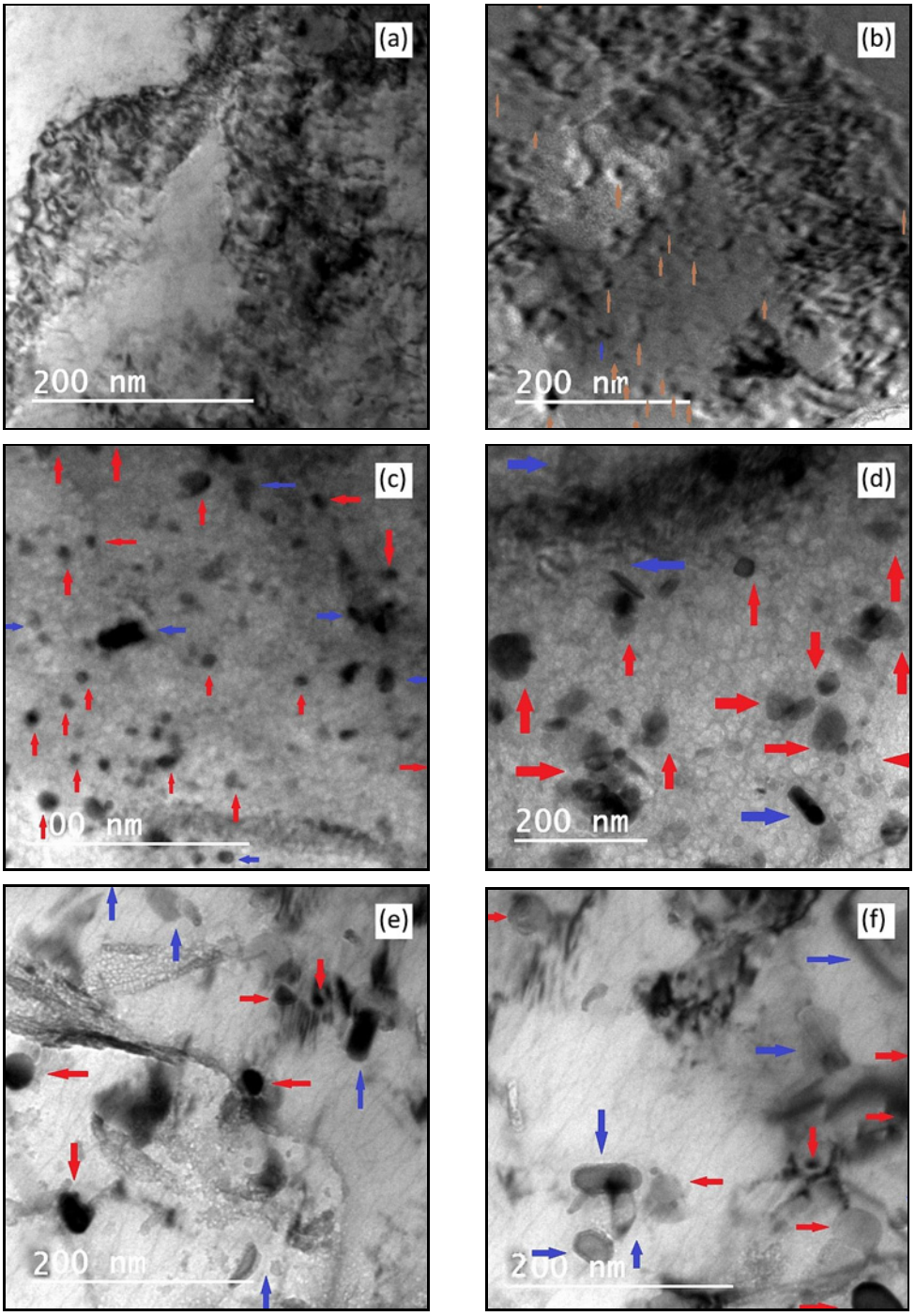


Fig. 5. TEM micrograph of (a) CR, (b) CR + 100 °C, (c) CR + 150 °C, (d) CR + 200 °C, (e) CR + 300 °C, and (f) CR + 350 °C.

of low-angle grain boundaries (LAGB). The HAGB is defined as the grain boundaries with a misorientation angle higher than 15°. The CR specimen showed a decrease in the HAGB fraction by 73.6 % to 0.154 and an increase in LAGB, which is indicative of the formation of subgrain structure due to high dislocation density induced during the CR treatment, and suppression of dynamic recovery during cryogenic temperature. During the annealing treatment, the fraction of HAGB increases with an increase in the annealing temperature. As the annealing temperature increases from 100 to 150, 250, and 350 °C, the fraction of HAGB increases from 0.141, 0.150, 0.320, and 0.422, respectively. This increase in the HAGB fraction can be accredited to the dynamic recovery at elevated temperatures during PA. The PA treatment leads to the dislocation annihilation, thereby reducing the dislocation density. The regions with high dislocation formed during the SPD

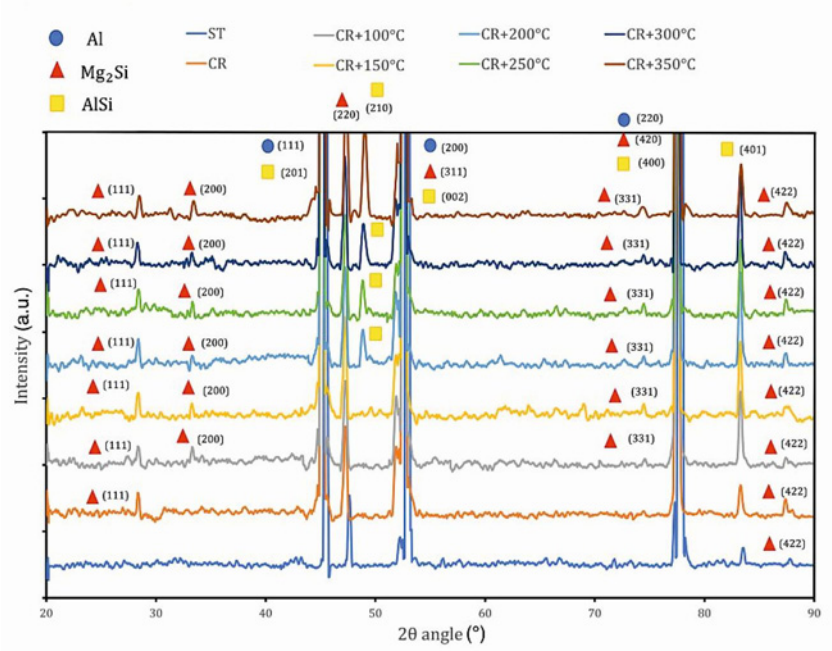


Fig. 6. XRD results for various processing conditions.

process lead to the formation of subgrains, which are subsequently converted into the LAGB due to rearrangement and annihilation of dislocation. The LAGB was converted into HAGB during PA treatment due to subgrain rotation and dislocation migration at elevated temperatures.

### 3.1.2. TEM

The microstructural topographies, such as grain size and precipitates in CR samples, were below the resolution of the optical microscope. Hence, further characterisation of CR and post-annealed samples was done using TEM analysis. Figure 5 demonstrates the TEM micrograph of CR and post-annealed samples. Samples cryorolled to 90 % thickness reduction (a true strain of 2.3) exhibit the elongated microstructure consisting of high dislocation content and subgrains, as can be observed in Fig. 5a. High deformation imparted to the samples during CR results in the generation of high-deformation zones consisting of fine subgrains and high dislocation density. The regions with high dislocation tangles rearrange themselves to form subgrains. When CR samples were subjected to annealing at 100 ℃, dislocation density and the number of subgrains reduced, as seen in Fig. 5b. As the annealing temperature increases beyond 150 ℃, the dislocation density decreases significantly; grain size increases due to recovery, and cell boundaries evolve into subgrain boundaries, as depicted in Fig. 5d. The deformation zones formed during cryorolling act as nucleation sites for recrystallisation; this process is widely recognised as "particle-simulated nucleation (PSN)" [23]. As the annealing temperature increases to 350 ℃, most of the dislocations in the sample are recovered, relaxed, and transformed into subgrains size, as can be observed from Fig. 5f. It might be owing to the accelerated recovery and recrystallisation processes happening in this temperature range. The evolution of the precipitate in annealing can also be observed in TEM micrographs. In CR samples, the precipitates are negligible. Annealing at 100 ℃ resulted in the formation of fine spherical precipitates throughout the sample. When the annealing temperature rises to 150 ℃, the sample exhibits a mixture of fine and coarse spherical and needle-shaped precipitates. However, the amount of needle or rod-shaped precipitates (indicated by the blue arrow) is significantly lower than the spherical precipitates (denoted using the red arrow), as depicted in Figs. 5b–f. The volume fraction of the fine spherical precipitates increases to 100 ℃, but as the annealing temperature rises beyond 100 ℃, the precipitates become coarse and segregated. As the annealing temperature approaches 350 ℃, the dislocations become negligible, and the spherical and needle-shaped precipitates evolve into elongated rod-shaped precipitates, as presented in Fig. 5f.

### 3.1.3. XRD

The X-ray diffraction pattern of Al 6351 in ST, CR, PA (post-annealed) conditions is shown in Fig. 6. In Al 6351 alloy, two different types of precipitates, namely $\delta$ ($Al_2Si$) and $\alpha$ ($Mg_2Si$), were observed. X-ray pattern of solution-treated and cryorolled samples show a small amount of both $\delta$ and $\alpha$ precipitates.

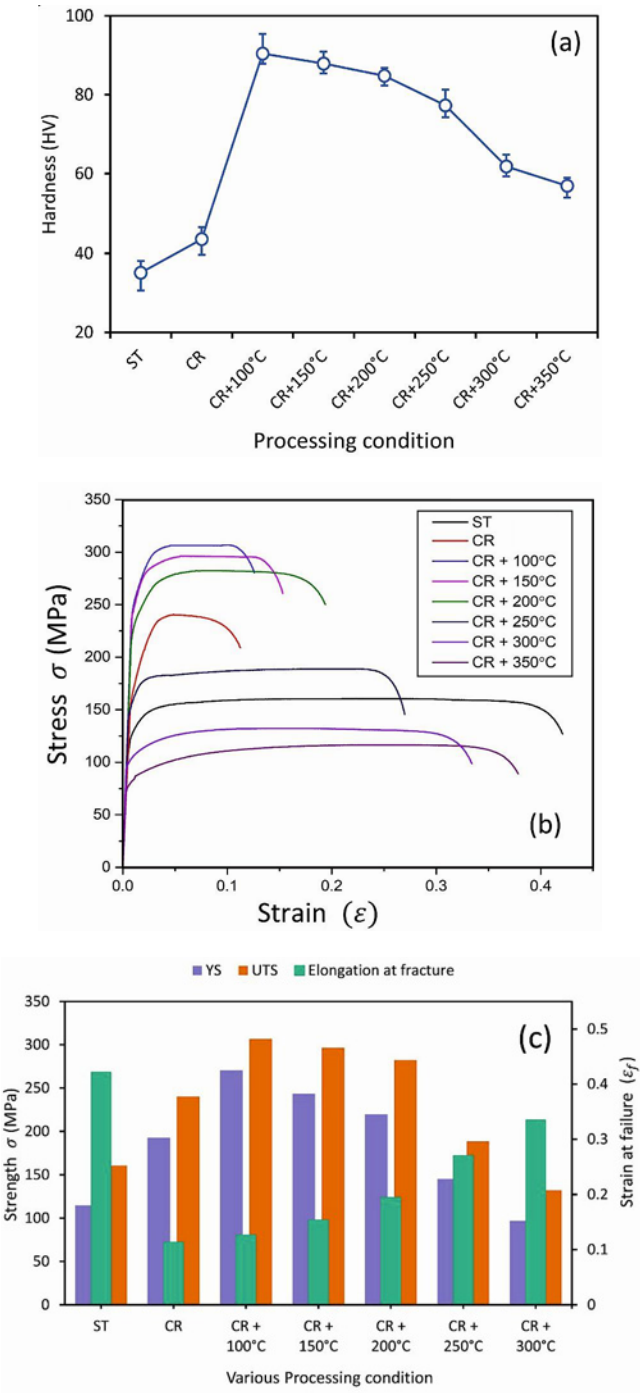


Fig. 7. (a) Variation in the hardness of Al 6351 alloy under ST, CR, and annealed conditions, (b) stress-strain curve of Al 6351 in various processing conditions, and (c) variation in UTS, YS, and strain at fracture in different processing conditions.

This might be because the precipitates get dissolved back into the metal during solution treatment, and the temperatures in the subsequent cryorolling treatment are insufficient for precipitate evolution. CR sample annealing leads to precipitating development, as witnessed in the TEM analysis. In CR + 100 ℃ and CR + 150 ℃, $\alpha$ precipitate is the primary precipitate, and $\delta$ precipitate is present in trace amounts. As the annealing temperature increases to 200 ℃, the $\delta$ precipitate evolves within the Al 6351 samples. Further increasing the annealing temperature to 350 ℃ leads to a corresponding increase in the fraction of $\delta$ precipitate.

### 3.2. Mechanical properties

The effect of CR and post-rolled annealing treatment on the hardness of the Al 6351 alloy is depicted in Fig. 7a. Samples cryorolled to a true strain of 2.3 show 24 % higher hardness compared to the solution-treated samples (35.1 HV in ST samples compared to 43.6 HV in CR samples). This upsurge can be accredited to the high dislocation density of CR samples, as witnessed in the TEM micrograph in Fig. 5, and the suppression of dislocation movement and cross slip at cryogenic temperature. Annealing treatment further escalates the hardness of Al 6351 alloy. The hardness of the heat-treatable Al alloys can be maximized by optimizing the interaction between conflicting factors, namely precipitate formation, recovery of dislocation at higher temperatures, and substructure coarsening [24]. A peak hardness of 90.4 HV is obtained at 100 ℃ temperature due to the formation of the fine uniformly distributed spherical precipitates throughout the metal matrix as observed in the TEM micrograph and XRD pattern displayed in Fig. 6. As the temperature of annealing rises beyond 150 ℃, the hardness decreases steadily with an increase in the temperature. This fall in the hardness can be attributed to the recovery of the dislocations and structure coarsening.

The stress-strain curve of the Al 6351 in ST, CR, and post-annealed conditions is shown in Fig. 7b. Tensile and hardness behaviour are shown in Table 2. The tensile strength is augmented from 160 to 240 MPa after cryorolling treatment with a 90 % thickness reduction. This substantial improvement in tensile strength is due to the high dislocation density in CR samples due to the suppression of cross slip of dislocation at liquid nitrogen temperature [14] and the UFG microstructure of CR alloys, as observed in the TEM micrograph. However, this rise in tensile strength coincides with a decrease in ductility, dropping from 42.05 to 11.26 %. Other researchers [13] and [21] made similar annotations on the cryorolling of Al-Mg-Si and Al-Cu-Si, respectively. The tensile behaviour of post-annealed Al 6351 shows similar trends observed in the hardness behaviour in corresponding conditions. The maximum tensile strength of 307 MPa is observed in samples annealed at 100 ℃, owing to the formation of fine, coherent, spherical $Mg_2Si$ precipitates during the annealing treatment. The ductility of the samples is also improved from 11.26 % in CR samples to 12.57 % in CR + 100 ℃ samples, as shown

Table 2. Mechanical characteristics of Al 6351 alloy under dissimilar processing conditions

| Processing condition | Yield strength (MPa) | Ultimate tensile strength (MPa) | Strain at fracture | Hardness HV |
|---|---|---|---|---|
| ST | 115 ± 3 | 160 ± 8 | 0.4205 ± 0.15 | 35.1 ± 2.7 |
| CR | 192 ± 5 | 240 ± 11 | 0.1126 ± 0.2 | 43.6 ± 3.2 |
| CR + 100 °C | 270 ± 7 | 307 ± 9 | 0.1257 ± 0.07 | 90.4 ± 1.3 |
| CR + 150 °C | 243 ± 10 | 296 ± 7 | 0.1530 ± 0.12 | 87.9 ± 2.1 |
| CR + 200 °C | 219 ± 9 | 282 ± 4 | 0.1939 ± 0.21 | 84.8 ± 4.5 |
| CR + 250 °C | 145 ± 6 | 188 ± 6 | 0.2698 ± 0.13 | 77.3 ± 1.8 |
| CR + 300 °C | 97 ± 11 | 132 ± 13 | 0.3341 ± 0.14 | 61.8 ± 3.8 |
| CR + 350 °C | 71 ± 8 | 116 ± 8 | 0.3784 ± 0.09 | 56.9 ± 5.5 |

in Fig. 7c. This augmentation in ductility is owing to the coarsening of grain size and reduction in the dislocation density at elevated temperatures. An increase in the annealing temperature to 150 °C resulted in a slight decrease in the UTS (from 307 MPa for CR + 100 °C to 296 MPa for CR + 150 °C sample condition), whereas the ductility increased from 12.57 to 15.30 %. This slight drop in ductility indicates that the softening effect or recovery of the dislocation becomes the dominant effect compared to the precipitation hardening. When the annealing temperature is augmented beyond 200 °C, a sudden decrease in tensile strength is observed, whereas the ductility is improved significantly. These changes in tensile behaviour are due to the coarse equiaxed microstructure due to recrystallisation during annealing; the coherency of the precipitates with the matrix is lost beyond 200 °C, and the size of the precipitates increases. Similar findings were reported for Al 6061 alloy [25].

#### *3.2.1. Fractograph after tensile test*

Fractured surface morphology of ST, CR, and post-annealed samples after tensile testing were examined using SEM and are presented in Fig. 8a. The fractograph of ST Al 6351 alloy shows well-developed spherical dimples (indicated by the yellow colour in Fig. 8). This type of fracture surface is a characteristic feature of ductile fracture [21]. After cryorolling, the fracture mode is revamped to a mixed-mode fracture. The fractured surface of CR samples shows a combination of fine spherical dimples and a small proportion of flat facets, as shown in Fig. 8b. These flat facets indicate brittle fracture and appear in CR samples due to strain hardening of Al 6351 alloy during cryorolling. These fine spherical dimples indicate the UFG microstructure of the cryorolled samples. The fracture mode remains mixed in samples subjected to annealing at 100 °C, but the number of flat facets is significantly reduced. The size of the dimples is considerably greater when compared with CR samples as the annealing temperature is augmented from 100 to 350 °C, the size of dimples increases, and the volume fraction of flat facets decreases. This effect is reflected in the increase in ductility of the post-annealed samples, as discussed in the previous section. The decrease in volume fraction of the flat facets also indicates the shift in the fracture mode from a mixed mode in CR + 100 °C to predominantly ductile fracture in CR + 350 °C.

### *3.3. Fracture toughness*

Fracture toughness is one of the most crucial characteristics for designing any component in high-strength applications, as it indicates the life of a component in the presence of a crack or discontinuity. Hence, fracture studies of various heat-treatable and non-heat-treatable aluminium alloys have been widely studied by researchers for the past few decades [21, 26]. The stress intensity factor and the $J$ integral are two of the most critical parameters that can be used to estimate the deformation behaviour of metals. However, the dimension required for fracture toughness testing is hard to achieve in cryorolling. In samples with small-scale yielding near the crack tip, the thickness of the samples must satisfy the ASTM standard E399-05 for plane-strain fracture toughness [21]. Hence, the literature on fracture toughness in cryorolling is scarce. UFG Al 6351 alloy is subjected to fracture toughness testing using "single edge notch bending (SENB)" tests.

#### *3.3.1. Plane strain fracture toughness*

Plane strain fracture toughness ($K_Q$) is a characteristic of the linear elastic fracture mechanics (LEFM) approach. This approach does not account for the ductility; hence, in LEFM, the dimensions of plastic zones at the crack tip are minimal. As per "ASTM standard 399," the minimum thickness obligatory for $K_Q$ is given by:

$$B = 2.5 \left( \frac{K_{IC}}{\sigma_0} \right)^2, \tag{2}$$

where $\sigma_0$ is the 0.2 % offset yield strength. Maximum

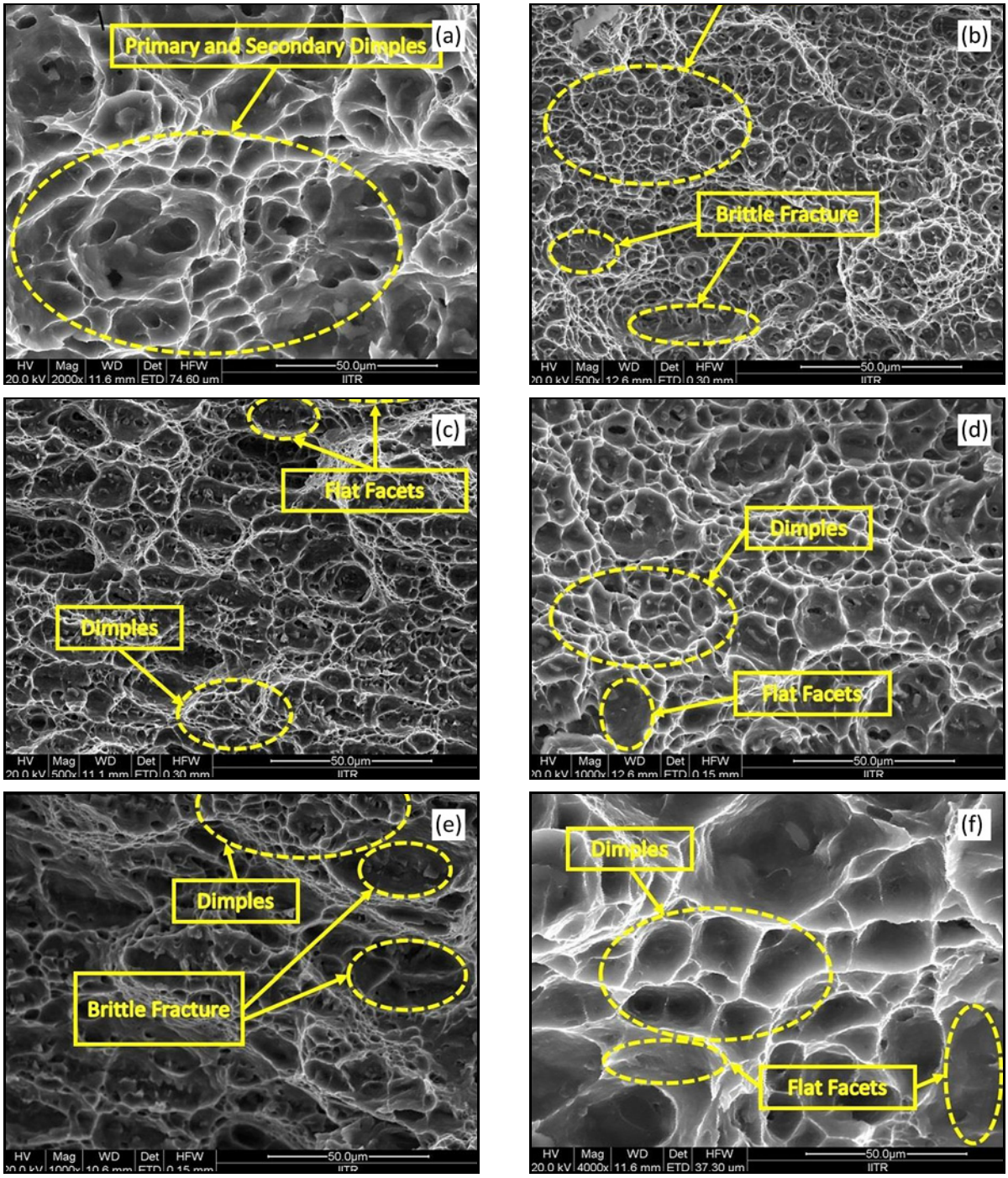


Fig. 8. Fractured surface morphology for Al 6351 alloy after tensile testing: (a) ST, (b) CR, (c) CR + 100 °C, (d) CR + 250 °C, (e) CR + 300 °C, and (f) CR + 350 °C.

thickness ($B$) calculated by this equation should be greater than pre-crack length ($a$) and length of the unbroken ligament (i.e., $W$-$a$) [27]:

$$K_{\mathrm{Q}} = \frac{P_{\mathrm{Q}}}{B}\frac{S}{W^{\frac{3}{2}}}\left[2.9\left(\frac{a}{W}\right)^{\frac{1}{2}} - 4.6\left(\frac{a}{W}\right)^{\frac{3}{2}} + 21.8\left(\frac{a}{W}\right)^{\frac{5}{2}} - 37.6\left(\frac{a}{W}\right)^{\frac{7}{2}} + 38.7\left(\frac{a}{W}\right)^{\frac{9}{2}}\right]. \quad (3)$$

According to the above equation, $K_{\mathrm{Q}}$ for solution treated Al 6351 sample comes out to be 5.88 MPa$\sqrt{\mathrm{m}}$. The maximum thickness $B$ is evaluated as 5.79 mm. Maximum thickness $B$ obtained for ST samples is more significant than $a$, and $(W - a)$. Hence, the samples used in the experiments do not meet plane-strain criteria, which means fracture toughness calculated by the above equation is known by apparent fracture toughness. The fracture toughness parameters of Al

Table 3. Fracture toughness of different conditions

| Processing condition | $K_Q$ (MPa$\sqrt{m}$) | $K_{ee}$ (MPa$\sqrt{m}$) | $J$ integral (kJ m$^{-2}$) |
|---|---|---|---|
| ST | 5.88 ± 0.66 | 11.97 ± 0.47 | 6.06 ± 0.62 |
| CR | 8.46 ± 1.10 | 16.39 ± 1.63 | 9.53 ± 1.62 |
| CR + 100 °C | 11.19 ± 1.32 | 19.20 ± 1.57 | 12.51 ± 2.52 |
| CR + 150 °C | 10.98 ± 0.75 | 20.09 ± 0.38 | 13.76 ± 1.61 |
| CR + 250 °C | 10.46 ± 1.26 | 18.26 ± 1.77 | 11.84 ± 1.47 |
| CR + 300 °C | 6.28 ± 0.68 | 13.17 ± 0.78 | 7.57 ± 1.57 |
| CR + 350 °C | 5.51 ± 0.98 | 10.28 ± 1.28 | 4.83 ± 1.52 |

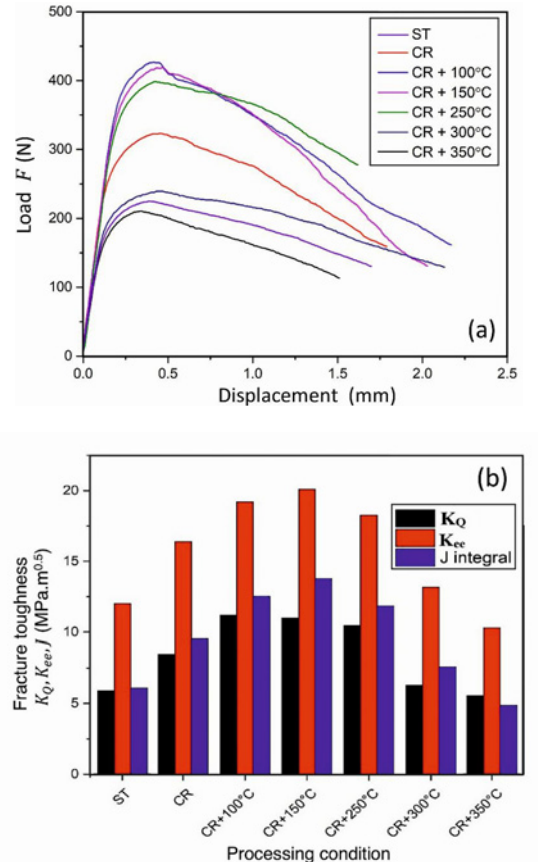


Fig. 9. (a) Load vs. extension curve in different processing conditions and (b) fracture measuring parameters of Al 6351 in distinct processing conditions.

6351 in distinct processing conditions are shown in Fig. 9b and tabulated in Table 3.

The apparent fracture toughness is an accurate indicator of resistance for crack initiation in the material because the crack initiation mainly depends on the strength of the material and not on the ductility of the material. So, the LEFM approach can determine the resistance during the crack initiation phase. The $K_Q$ of the cryorolled sample was 43.8 % higher when compared with ST samples. This change can be accredited to UFG microstructure and high dislocation density of CR samples, as observed in the TEM results in Fig. 5. A similar observation has been made for various UFG alloys processed by different SPD processes [28]. Annealing the CR samples to 100 °C further increases the fracture toughness by 32 % (8.46 MPa$\sqrt{m}$ in CR samples to 11.19 MPa$\sqrt{m}$ in CR + 100 °C samples). This increase is attributed to the formation of $\delta$ precipitate during the annealing process, as confirmed by XRD analysis. The fracture toughness of heat-treatable aluminium alloys is influenced by the shape, size, and distribution of precipitates. Fine precipitates that are evenly distributed throughout the metal matrix enhance fracture toughness. As the annealing temperature increases from 150 to 350 °C, $K_Q$ decreases. A similar trend can be observed in the tensile strength of the Al 6351 samples.

### 3.3.2. Equivalent energy fracture toughness

In this study, equivalent energy fracture toughness ($K_{ee}$) was examined according to the "ASTM E-992 standard". The thickness of the sample cryorolled at 90 % thickness reduction is relatively small, and hence it is challenging to satisfy the dimension required for fracture toughness evaluation. So, in samples with thickness lower than the minimum limit, the equivalent load ($P_E$) is used instead of the provisional load ($P_Q$) to evaluate the fracture toughness. Equivalent load $P_E$ was determined using the following equation:

$$P_E = P_L \sqrt{\frac{A_T}{A_L}}, \tag{4}$$

where $P_L$ stands for load up until the load versus extension curve is linear. $A_L$ denotes the area of the load-extension curve in the linear range, while $A_T$ represents the area up to peak load. Equivalent energy fracture toughness $K_{ee}$ is evaluated by using the following formula, as reported in various research studies [6, 21]:

$$K_{ee} = \frac{P_E}{B}\frac{S}{W^{\frac{3}{2}}}\left[2.9\left(\frac{a}{W}\right)^{\frac{1}{2}} - 4.6\left(\frac{a}{W}\right)^{\frac{3}{2}} + 21.8\left(\frac{a}{W}\right)^{\frac{5}{2}} - 37.6\left(\frac{a}{W}\right)^{\frac{7}{2}} + 38.7\left(\frac{a}{W}\right)^{\frac{9}{2}}\right]. \tag{5}$$

The trend observed in $K_{ee}$ in different processing conditions is the same as the trend in $K_Q$ discussed in the previous section. $K_{ee}$ of Al 6351 in different processing conditions is shown in Fig. 9b and Table 3.

#### 3.3.3. J integral

$J$ integral is the EPFM (elastic-plastic fracture mechanics) parameter. EPFM approach deals with the effect of ductility in a metal matrix. The crack initiation phase of the fracture primarily depends on the strength, and hence, the stress intensity factor can be used as a measure to predict the resistance of material for crack initiation; however, the crack propagation is influenced by both strength and ductility of the material [6, 17, 29, 30]. Since the EPFM approach considers the effect of ductility, the $J$ integral determines the crack growth resistance under static loading. In this current study, the $J$ integral is calculated as per ASTM 1820-15a standard [21] and is represented by the following equation:

$$J = \frac{2A}{Bb}, \tag{6}$$

where $A$ is the area under the load-extension curve, $b$ is the unbroken ligament's length, and $B$ is the thickness of the specimen. After cryorolling, the $J$ integral of the Al 6351 increases by 57.3 % (6.06 kJ m$^{-2}$ in ST to 9.53 kJ m$^{-2}$ in the CR sample). This upsurge in $J$ integral is due to a rise in tensile strength due to the formation of the UFG microstructure. Annealing of the CR samples leads to further increase in the $J$ integral. The $J$ integral of CR + 100 ℃ samples is 12.51 kJ m$^{-2}$. This increase in fracture toughness can be attributed to the development of fine spherical precipitates throughout the matrix, as shown in Fig. 5b. As the annealing temperature increases to 150 ℃, the $J$ integral increases to 13.76 kJ m$^{-2}$. This increase in $J$ integral is due to the combined strength and ductility. The strength of CR + 150 ℃ is lower compared to the CR + 100 ℃ samples, but the increase in ductility counteracts the impact of the decrease in strength on the $J$ integral. However, as the annealing temperature rises beyond 150 ℃, the effect of the decline in strength on the $J$ integral becomes dominant compared to the increase in ductility. Hence, the value of the $J$ integral reduces with an increase in annealing temperature.

#### 3.3.4. Fractograph after 3-PB test

The morphology of the fracture surface of the 3-PB test specimen in different processing conditions was studied by SEM microscopy and shown in Fig. 10. Fractograph of solution-treated samples shows coarse dimples uniformly distributed across the fracture surface. Researchers also made similar observations for other aluminium alloys [6, 21]. In the present research, the three-point bend test specimen was loaded in Mode-I type loading, in which the crack propagation is at right angles to the loading direction, and this Mode-I loading introduces triaxiality in the vicinity of the crack-tip and results in ductile tearing [6].

The fracture surface of cryorolling samples shows a combination of very fine dimples and flat facets, as shown in Fig. 10b. The lower dimension of dimples in the cryorolling samples can be accredited to the evolution of the UFG microstructure of the cryorolled Al 6351 alloy. Figure 10c shows the SEM fractograph of CR samples subjected to annealing at 100 ℃. Numerous fine dimples can be observed in the SEM results of CR + 100 ℃ samples. At 100 ℃, the fracture parameters were higher than the CR samples due to precipitation strengthening. As the annealing temperature is augmented to 150 ℃, the size of the dimple increases. Fracture toughness parameters corresponding to the EPFM approach are higher at this temperature than those for CR + 100 ℃ samples; this indicates a higher crack propagation period due to higher ductility. With further enhancement in annealing temperature from 200 to 350 ℃, the fracture toughness starts decreasing. SEM fractography of the samples in this temperature range shows a higher volume fraction of brittle facets compared to the lower annealing temperature. As the annealing temperature increases, the volume fraction of the brittle facets also upsurges, as revealed in Figs. 10e,f. Brittle facets indicate that the crack propagation phase is minimal at the higher annealing temperature. This might be due to coarse precipitates at higher annealing temperatures, as revealed in the TEM micrograph. A similar observation was made for other aluminium alloys [6, 21].

## 4. Finite element modelling

The tensile and fracture behaviour was simulated using finite element analysis (FEM) and extended finite element analysis (XFEM). The FEM and XFEM approach allows us to simulate complex geometries, and boundary conditions, making it suitable to predict the properties without doing the experiments. These simulations offer a cost-effective alternative to the actual experiments and can be extended to predict the structural integrity of the components.

### 4.1. Tensile simulation

The tensile simulation was performed on *ABAQUS 6.1 software*. The elastic region was modelled using the elastic constant, i.e., Poisson's ratio ($\mu$) and Young's modulus ($E$). The plastic region was defined using the plastic stress versus plastic strain data from the experimental stress-strain curve. The failure criteria were

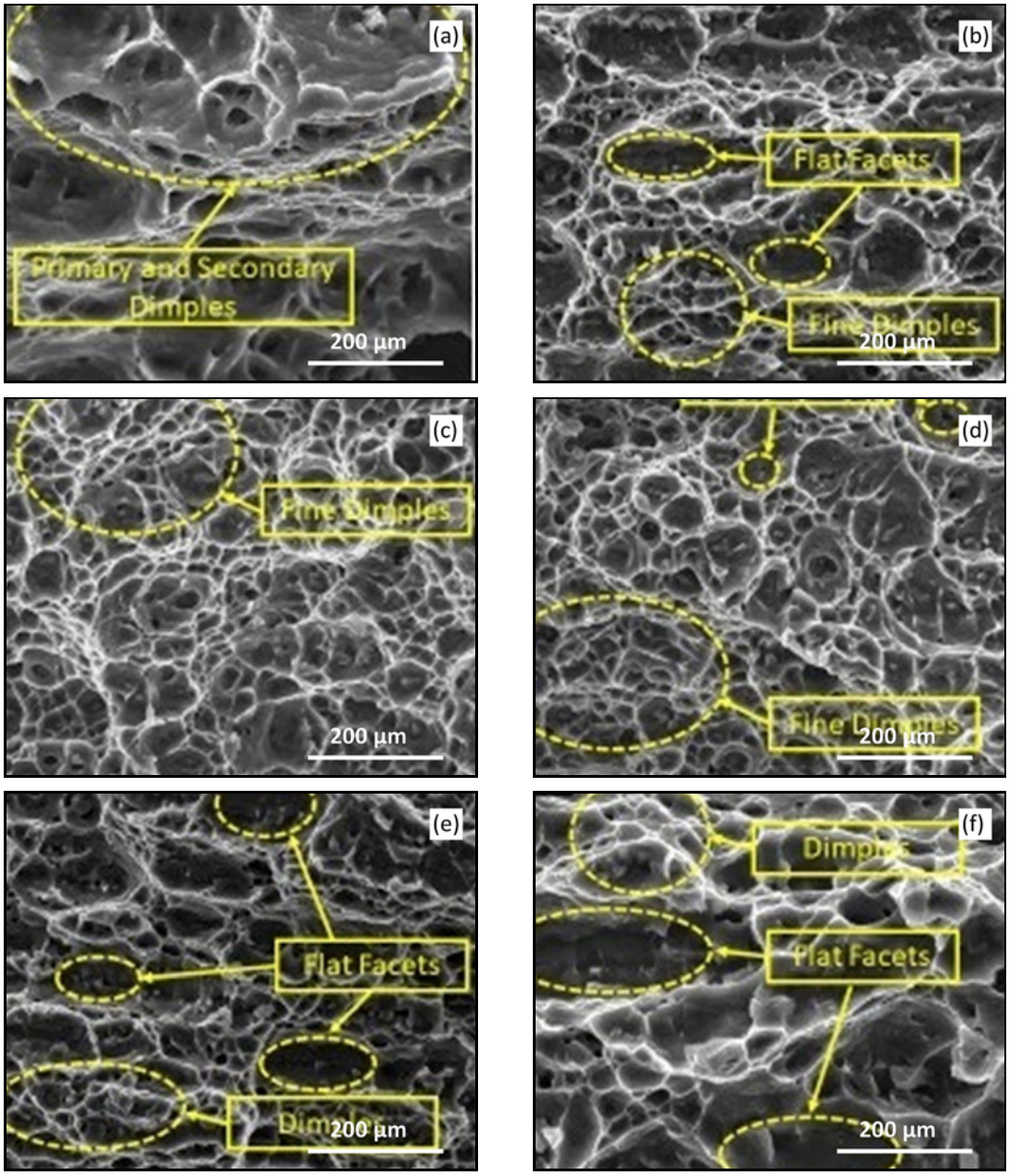


Fig. 10. Fractured surface morphology of Al 6351 alloy after 3-PB test: (a) ST, (b) CR, (c) CR + 100 °C, (d) CR + 150 °C, (e) CR + 250 °C, and (f) CR + 350 °C.

defined using fracture strain and displacement at fracture. The mesh containing C3D8R was used, and the mesh sensitivity analysis was performed to get the optimum mesh size. One side of the tensile specimen was fixed, and the other was loaded with displacement-controlled loading, as illustrated in Fig. 11a. Figure 11a shows the von Mises stress contour of the tensile specimen during loading and necking. The von Mises stress during loading shows uniform stress distribution in the gauge section. This is because the samples are considered homogeneous. Figure 11b shows that the tensile properties predicted using the finite element analysis (FEA) are in tandem with the experimentally observed properties. This fact is further demonstrated by the comparison of the ultimate tensile strength in experimental and simulated conditions in Fig. 11c. The red line indicates the perfect prediction of the ultimate tensile strength, and all the points are very close to the red line, indicating a very good prediction of ultimate tensile strength.

### *4.2. Three-point bend test*

The three-point bend test was simulated using the XFEM approach in *ABAQUS 6.1 software*. The conventional FEA requires the alignment of the crack

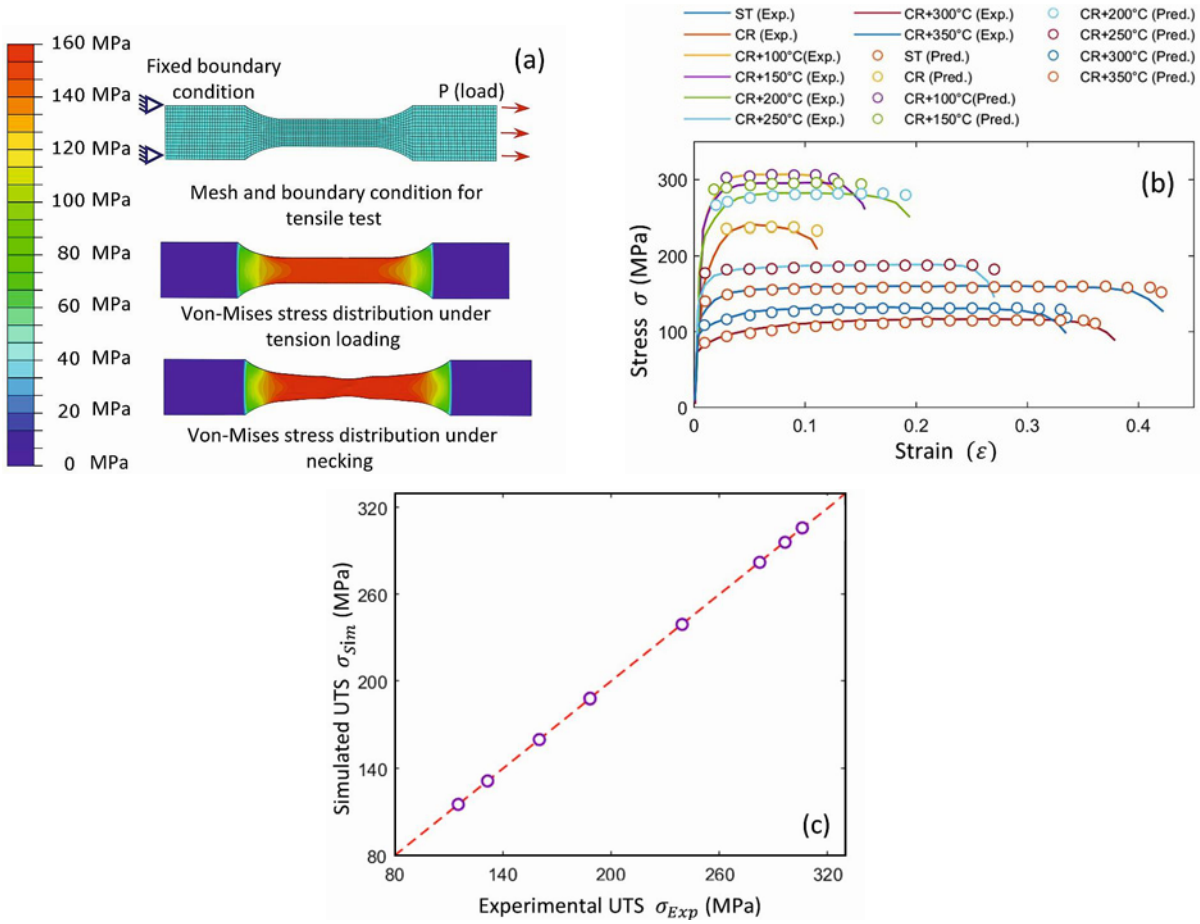


Fig. 11. (a) Details of finite element analysis such as mesh and boundary condition for tensile simulation, von Mises stress distribution during loading, and necking (colour bar showing the stress value), (b) comparison of the experimental and simulated stress-strain curve, and (c) comparison of simulated versus experimental UTS.

edge with the element edge, leading to the requirement of crack growth during crack growth. The XFEM approach permits crack growth through the elements, thereby reducing computational time by eliminating the requirement for remeshing. The XFEM approach uses two additional functions, i.e., the crack tip enrichment and Heaviside functions. The crack surface was enriched using the Heaviside enrichment function $H(x)$, taking a value of –1 below and +1 above the crack. The crack tip was enriched with crack tip enrichment function ($\varphi(x)$), which can be defined as [17, 31, 32]:

$$\varphi_{1-4}(x) = r^l \sin\left(\frac{\theta}{2}\right), r^l \cos\left(\frac{\theta}{2}\right), \quad (7)$$
$$r^l \sin\left(\frac{\theta}{2}\right)\sin(\theta), r^l \cos\left(\frac{\theta}{2}\right)\sin(\theta),$$

where (r, $\theta$) is a polar coordinate system. The exponent $l$ is 0.5 for the LEFM approach and $1/(1+n)$ for the EPFM approach ($n$ is the hardening exponent). The displacement in the XFEM is defined as:

$$u^h(x) = \sum N_I(x)^N_{I=1,J-1,K-1}[U_i(x) + H(x)a_j + \sum \varphi(x) b^x_K]^{x=4}_{x=1}. \quad (8)$$

The first element, $U(x)$, is the conventional FEA displacement term calculated for the whole surface. The second ($H(x)$) and third element ($\varphi(x)$) correspond to the enrichment at the crack and are calculated for the elements associated with the crack. The rigid cylindrical pins were modelled for support and loading. The fixed and displacement loading conditions are depicted in Fig. 12a. The input for the elastic and plastic region for the three-point bend simulation was the same as the tensile inputs, and the maximum fracture criteria were used as the failure criteria. The contact between rigid pins and the specimen was defined as hard normal contact. The Von Mises stress distribution at various stages of crack propagation is shown in Fig. 12a. The stress is concentrated in the areas surrounding the loading and supporting pins. The stress distribution about the crack surface is symmetric, a characteristic feature of mode I type loading.

Table 4. Comparison of the experimental and simulated fracture toughness

| | $K_Q$ (MPa$\sqrt{m}$) | | $J$ integral (kJ m$^{-2}$) | |
|---|---|---|---|---|
| | Exp. | Sim. | Exp. | Sim. |
| ST | 5.88 ± 0.66 | 5.89 | 6.06 ± 0.62 | 4.88 |
| CR | 8.46 ± 1.10 | 8.4 | 9.53 ± 1.62 | 7.69 |
| CR + 100 °C | 11.19 ± 1.32 | 11.19 | 12.51 ± 2.52 | 14.70 |
| CR + 150 °C | 10.98 ± 0.75 | 10.87 | 13.76 ± 1.61 | 13.89 |
| CR + 250 °C | 10.46 ± 1.26 | 10.26 | 11.84 ± 1.47 | 12.44 |
| CR + 300 °C | 6.28 ± 0.68 | 6.28 | 7.57 ± 1.57 | 9.06 |
| CR + 350 °C | 5.51 ± 0.98 | 5.51 | 4.83 ± 1.52 | 5.43 |

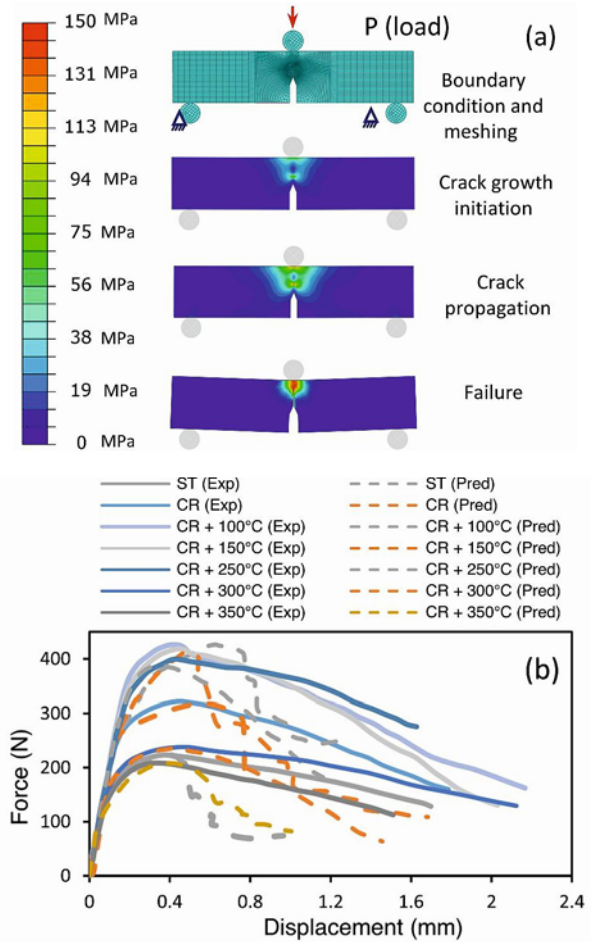


Fig. 12. (a) Details regarding the finite element analysis such as mesh and boundary conditions for three-point bend specimen, stress distribution in different regions of crack growth (colour bar showing the stress value), and (b) comparison of experimental and simulated force versus displacement curves.

The comparison of the load versus displacement diagram of the simulated curve with the experimental curve is shown in Fig. 12b. The peak load predicted using XFEM is in tandem with the experimental observation, as shown in Table 4. The fracture toughness, i.e., stress intensity factor ($K_Q$) and $J$ integral of the experimental and simulated curve, is shown in Table 4. The simulated fracture toughness aligns well with the experimental observations.

## 5. Conclusions

This study investigates the mechanical and microstructural behaviour of solution-treated (ST), cryorolled (CR), and post-annealed (PA) Al 6351 alloy, revealing that CR treatment significantly enhances the mechanical properties, increasing tensile strength by 50 % (from 160 MPa in ST samples compared to the 240 MPa in CR). This increment can be primarily attributed to the formation of ultrafine-grained microstructure and the evolution of high dislocation density due to the suppression of dynamic recovery at cryogenic temperature. Post-rolling annealing at 100 °C leads to the formation of spherical and needle-shaped precipitates, resulting in a 27.92 % increase in tensile strength (from 240 to 307 MPa), a 107.5 % improvement in hardness (from 43.6 to 90.4 HV), and an 11.6 % increase in ductility, while higher annealing temperatures (150–350 °C) cause a decrease in tensile strength and hardness due to the dominant recovery effect. Cryorolling also improves fracture toughness by increasing crack initiation resistance, with further enhancement observed at 100 °C due to precipitate development, shifting the fracture mechanism from ductile in ST samples to mixed mode in CR and annealed samples, and predominantly ductile at higher annealing temperatures. Tensile simulation predictions for yield strength and ultimate tensile strength are within 1.7 % of experimental values, and fracture toughness predictions using the XFEM approach align well with experimental observations.

## References

[1] R. Singh, Crack growth analysis of room temperature rolled (RTR) 6351 Al alloys by XFEM, Int.

J. Microstruct. Mater. Prop. 10 (2015) 239–258. https://doi.org/10.1504/IJMMP.2015.072919
[2] S. Kar, S. Chakraborty, V. Dey, S. K. Ghosh, Optimization of surface roughness parameters of Al-6351 alloy in EDC process: A Taguchi Coupled Fuzzy Logic approach, J. Inst. Eng. Ser. C 98 (2017) 607–618. https://doi.org/10.1007/s40032-016-0297-y
[3] S. Gairola, R. Jayaganthan, J. Ajay, Laser powder bed fusion on Ti modified Al 2024 alloy: Influence of build orientation and T6 treatment on mechanical behaviour, microstructural features and strengthening mechanisms, Mater. Sci. Eng. A 896 (2024) 146296. https://doi.org/10.1016/j.msea.2024.146296
[4] S. Gairola, R. Jayaganthan, Influence of heat treatment, microstructure evolution, and damage mechanism on high cycle fatigue behaviour of additively manufactured Ti-modified Al 2024 alloy, Mater. Charact. 203 (2023) 113047. https://doi.org/10.1016/j.matchar.2023.113047
[5] P. Nageswara Rao, R. Jayaganthan, Effects of warm rolling and ageing after cryogenic rolling on mechanical properties and microstructure of Al 6061 alloy, Mater. Des. 39 (2012) 226–233. https://doi.org/10.1016/j.matdes.2012.02.010
[6] S. Gairola, A. Joshi, B. Gangil, P. Rawat, R. Verma, Correlation of tensile properties and fracture toughness with microstructural features for Al-Li 8090 alloy processed by cryorolling and post-rolled annealing, Trans. Indian Inst. Met. 72 (2019) 1743–1755. https://doi.org/10.1007/s12666-019-01641-z
[7] R. Kapil, A. Joshi, R. Jayaganthan, S. Gairola, R. Verma, Improvement of fracture toughness of ultra fine grained Al-Li 8090 alloy processed through multi axial forging, Mater. Res. Express. 6 (2019) 085064. https://doi.org/10.1088/2053-1591/ab1f9d
[8] A. V. Korznikov, Y. V. Ivanisenko, D. V. Laptionok, I. M. Safarov, V. P. Pilyugin, R. Z. Valiev, Influence of severe plastic deformation on structure and phase composition of carbon steel, Nanostructured Mater. 4 (1994) 159–167. https://doi.org/10.1016/0965-9773(94)90075-2
[9] F. Wetscher, A. Vorhauer, R. Stock, R. Pippan, Structural refinement of low alloyed steels during severe plastic deformation, Mater. Sci. Eng. A 387–389 (2004) 809–816. https://doi.org/10.1016/j.msea.2004.01.096
[10] A. Yamashita, Z. Horita, T. G. Langdon, Improving the mechanical properties of magnesium and a magnesium alloy through severe plastic deformation, Mater. Sci. Eng. A 300 (2001) 142–147. https://doi.org/10.1016/S0921-5093(00)01660-9
[11] V. Kumar, P. C. Gope, Experimental and computational investigation of fracture toughness of cryorolling processed Al-6082 alloys, Eng. Fail. Anal. 159 (2024) 108005. https://doi.org/10.1016/j.engfailanal.2024.108005
[12] N. Kumar, P. N. Rao, R. Jayaganthan, H. Brokmeier, Effect of cryorolling and annealing on recovery, recrystallisation, grain growth and their influence on mechanical and corrosion behaviour of 6082 Al alloy, Mater. Chem. Phys. 165 (2015) 177–187. https://doi.org/10.1016/j.matchemphys.2015.09.014
[13] S. K. Panigrahi, R. Jayaganthan, A study on the mechanical properties of cryorolled Al-Mg-Si alloy, Mater. Sci. Eng. A 480 (2008) 299–305. https://doi.org/10.1016/j.msea.2007.07.024
[14] N. Rangaraju, T. Raghuram, B.V. Krishna, K. P. Rao, P. Venugopal, Effect of cryo-rolling and annealing on microstructure and properties of commercially pure aluminium, Mater. Sci. Eng. A 398 (2005) 246–251. https://doi.org/10.1016/j.msea.2005.03.026
[15] K. K. Yogesha, N. Kumar, A. Joshi, R. Jayaganthan, S. K. Nath, A comparative study on tensile and fracture behavior of Al-Mg alloy processed through cryorolling and cryo groove rolling, Metall. Microstruct. Anal. 5 (2016) 251–263. https://doi.org/10.1007/s13632-016-0282-0
[16] N. Kumar, G. M. Owolabi, R. Jayaganthan, O. O. Ajide, Plane stress fracture toughness of cryorolled 6082 Al alloy, Theor. Appl. Fract. Mech. 95 (2018) 28–41. https://doi.org/10.1016/j.tafmec.2018.02.011
[17] S. Gairola, R. Jayaganthan, XFEM simulation of tensile and fracture behavior of ultrafine-grained Al 6061 alloy, Metals (Basel) 11 (2021) 1761. https://doi.org/10.3390/met11111761
[18] V. Balakrishnan, P. Roshan, S. Goel, R. Jayaganthan, I. V. Singh, Experimental and XFEM simulation of tensile and fracture behavior of Al 6061 alloy processed by severe plastic deformation, Metallogr. Microstruct. Anal. 6 (2017) 55–72. https://doi.org/10.1007/s13632-016-0332-7
[19] P. Das, I. V. Singh, R. Jayaganthan, Crack growth simulation of bulk and ultrafine grained 7075 Al alloy by XFEM, Int. J. Mater. Prod. Technol. 44 (2012) 252–276. https://doi.org/10.1504/IJMPT.2012.050192
[20] R. Thiyagarajan, A. Gopinath, Enhancement of mechanical properties of AA 6351 using Equal Channel Angular Extrusion (ECAE), Mater. Sci. Metall. Eng. 2 (2014) 26–30. https://doi.org/10.12691/msme-2-2-3
[21] A. Joshi, K. K. Yogesha, N. Kumar, R. Jayaganthan, Influence of annealing on microstructural evolution, precipitation sequence, and fracture toughness of cryorolled Al–Cu–Si alloy, Metall. Microstruct. Anal. 5 (2016) 540–556. https://doi.org/10.1007/s13632-016-0313-x
[22] M. K. Pathak, A. Joshi, K. K. S. Mer, R. Jayaganthan, Mechanical properties and microstructural evolution of bulk UFG Al 2014 alloy processed through cryorolling and warm rolling, Acta Metall. Sin. 32 (2019) 845–856. https://doi.org/10.1007/s40195-018-0849-7
[23] A. Rollett, F. Humphreys, G. S. Rohrer, M. Hatherly, Recrystallization and Related Annealing Phenomena: Second Edition, Elsevier, 2004. https://doi.org/10.1016/B978-0-08-044164-1.X5000-2
[24] M. R. Rezaei, M. R. Toroghinejad, F. Ashrafizadeh, Effects of ARB and ageing processes on mechanical properties and microstructure of 6061 aluminum alloy, J. Mater. Process. Technol. 211 (2011) 1184–1190. https://doi.org/10.1016/j.jmatprotec.2011.01.023
[25] P. N. Rao, D. Singh, R. Jayaganthan, Effect of annealing on microstructure and mechanical properties of Al 6061 alloy processed by cryorolling, Materials Science and Technology 29 (2013) 76–82. https://doi.org/10.1179/1743284712Y.0000000041
[26] G. T. Hahn, A. R. Rosenfield, Metallurgical factors af-

fecting fracture toughness of aluminum alloys, Metall. Trans. A 6 (1975) 653–668. https://doi.org/10.1007/BF02672285

[27] R. Z. Valiev, I. V. Alexandrov, R. K. Islamgaliev, Processing and Properties of Nanostructured Materials Prepared by Severe Plastic Deformation, In: Nanostructured Mater., Springer Netherlands, Dordrecht, 1998, pp. 121–142. https://doi.org/10.1007/978-94-011-5002-6_7

[28] A. Joshi, N. Kumar, K. K. Yogesha, R. Jayaganthan, S. K. Nath, Mechanical properties and microstructural evolution in Al 2014 alloy processed through multidirectional cryoforging, J. Mater. Eng. Perform. 25 (2016) 3031–3045. https://doi.org/10.1007/s11665-016-2126-0

[29] B. Farahmand, M. Aliabadi, Fracture mechanics of metals, composites, welds, and bolted joints: Application of LEFM, EPFM, and FMDM theory, Appl. Mech. Rev. 55 (2002) B71. https://doi.org/10.1115/1.1483354

[30] P. Kothiyal, A. Joshi, K. K. S. Mer, S. Gairola, Influence of $Al_2O_3$ and $Si_3N_4$ nano-particulates on fracture toughness behaviour of sintered aluminium, Trans. Indian Inst. Met. 75 (2021) 199–215. https://doi.org/10.1007/s12666-021-02411-6

[31] S. Gairola, J. Rengaswamy, R. Verma, A study on XFEM simulation of tensile, fracture toughness, and fatigue crack growth behavior of Al 2024 alloy through fatigue crack growth rate models using genetic algorithm, Fatigue Fract. Eng. Mater. Struct. 46 (2023) 2121–2138. https://doi.org/10.1111/ffe.13987

[32] S. Gairola, R. Jayaganthan, R. K. Singh, N. Kumar, J. Ajay, An investigation on damage tolerant design parameter of additively manufactured Al 2024: Fatigue crack growth rate and fracture toughness, Mater. Today Commun. 38 (2024) 108480. https://doi.org/10.1016/j.mtcomm.2024.108480